Characterization: SEM images with EDX spectra were obtained with a Leica S-440I microscope fitted with an EDX spectrometer and Link ISIS detector. TEM images were recorded with a JEOL JEM 3010 instrument operating at an accelerating voltage of 300 kV fitted with a Gatan charge-coupled device (CCD) camera. Powder XRD patterns were recorded using a Seifert XRD 3000 TT instrument. Thermogravimetric analysis of the samples was carried out on a Mettler Toledo TG-850 apparatus.

Received: March 13, 2005
Final version: May 4, 2005
Published online: September 29, 2005

[1] R. C. Haddon (Ed.), Special issue on "Carbon Nanotubes", *Acc. Chem. Res.* **2002**, *35*, 997.
[2] C. N. R. Rao, B. C. Satishkumar, A. Govindaraj, M. Nath, *ChemPhysChem* **2001**, *2*, 78.
[3] Y. Xia, P. Yang, Y. Sun, Y. Wu, B. Mayers, B. Gates, Y. Yin, F. Kim, H. Yan, *Adv. Mater.* **2003**, *15*, 353.
[4] C. N. R. Rao, F. L. Deepak, G. Gundiah, A. Govindaraj, *Prog. Solid State Chem.* **2003**, *31*, 5.
[5] *Chemistry of Nanomaterials* (Eds: C. N. R. Rao, A. Muller, A. K. Cheetham), Wiley-VCH, Weinheim, Germany **2004**.
[6] *Nanowires and Nanobelts — Materials, Properties and Devices* (Ed: Z. L. Wang), Kluwer Academic, Boston, MA **2003**.
[7] P. J. F. Harris, *Int. Mater. Rev.* **2004**, *49*, 31.
[8] J. Goldberger, R. He, S. Lee, Y. Zhang, H. Yan, H. Choi, P. Yang, *Nature* **2003**, *422*, 599.
[9] P. M. Ajayan, O. Stephan, P. Redlich, C. Colliex, *Nature* **1995**, *375*, 564.
[10] B. C. Satishkumar, A. Govindaraj, E. M. Vogl, L. Basumallick, C. N. R. Rao, *J. Mater. Res.* **1997**, *12*, 604.
[11] C. N. R. Rao, B. C. Satishkumar, A. Govindaraj, *Chem. Commun.* **1997**, 1581.
[12] B. C. Satishkumar, A. Govindaraj, M. Nath, C. N. R. Rao, *J. Mater. Chem.* **2000**, *10*, 2115.
[13] K. Hernadi, E. Ljubovic, J. W. Se, L. Forró, *Acta Mater.* **2003**, *51*, 1447.
[14] W.-Q Han, A. Zettl, *Nano Lett.* **2003**, *3*, 681.
[15] L. Fu, Z. Liu, Y. Liu, B. Han, J. Wang, P. Hu, L. Cao, D. Zhu, *Adv. Mater.* **2004**, *16*, 350.
[16] Y.-S. Min, E. J. Bae, K. S. Jeong, Y. J. Cho, J.-H. Lee, W. B. Choi, G.-S. Park, *Adv. Mater.* **2003**, *15*, 1019.
[17] Y. X. Liang, Y. J. Chen, T. H. Wang, *Appl. Phys. Lett.* **2004**, *85*, 666.
[18] C. Journet, W. K. Maser, P. Bernier, A. Loiseau, M. Lamy de la Chapelle, S. Lefrabt, P. Denierd, R. Lee, J. E. Fischer, *Nature* **1997**, *388*, 756.
[19] G. Gundiah, F. L. Deepak, A. Govindaraj, C. N. R. Rao, *Top. Catal.* **2003**, *24*, 137.
[20] G. Gundiah, F. L. Deepak, A. Govindaraj, C. N. R. Rao, *Chem. Phys. Lett.* **2003**, *381*, 579.

ZnO Inverse Opals by Chemical Vapor Deposition**

By *Beatriz H. Juárez*, *Pedro David García*, *Dolores Golmayo*, *Alvaro Blanco*, and *Cefe López**

Among materials for photonics, ZnO is probably one of the most promising candidates, leading the race for innovation in the next decade. Widely used in numerous applications such as piezoelectric transducers, solar cells, phosphors, and sensors, this wide-gap (3.4 eV) semiconductor has been shown to be a good alternative to other classic materials such us GaN or SiC as a short-wavelength light emitter.[1] Thanks to its large excitonic binding energy (60 meV), lasing at room temperature was demonstrated in thin ZnO films in the last decade.[2] Since then, different ZnO nanostructures have emerged in many different sizes, shapes, and geometries, e.g., nanowires,[3] nanobelts,[4] or nanoribbons,[5] improving its lasing efficiency and boosting its possibilities in photonics. If more efficient photonic structures are to be built, photonic crystals (PCs) are ideal systems for fabricating efficient light emitters due to their ability to manipulate light.[6] PCs present photonic gaps or pseudogaps, which could eventually lead to a reduction or even elimination of the spontaneous emission, enhancing light emission and lowering the threshold in future lasing devices. There are a number of examples of ZnO-based PCs in one,[7] two,[8] or three dimensions.[9] In three-dimensional (3D) opal-based PCs, ZnO infiltration of silica opals has been tackled by wet chemical methods,[10,11] and polymeric opals have also been infiltrated with ZnO by sol–gel[12] and electrochemical methods.[13]

There are different approaches to growing polycrystalline or epitaxial ZnO. Techniques involving the gas phase are the most widespread, due to the high quality epitaxial growth, and can be directly applied in industry. Furthermore, gas-phase methods have demonstrated their potential in conformal growth for the infiltration of high aspect ratio structures.[14–16] Atomic layer deposition (ALD)[16,17] provides atomic-scale thickness control of ZnO films by oxidation of metal–organic precursors such as diethyl zinc (DEZn) or dimethyl zinc (DMZn) (which are highly reactive in air) by alternating metal–organic and water exposures or pulses of a few seconds length in a binary reaction sequence. These methods have, however, never been used in porous environments such as opals even though they

[*] Dr. C. López, Dr. B. H. Juárez, P. D. García, Dr. D. Golmayo, Dr. A. Blanco
Instituto de Ciencia de Materiales de Madrid (CSIC)
C/Sor Juana Inés de la Cruz 3, ES-28049 Madrid (Spain)
E-mail: cefe@icmm.csic.es

[**] This work was partially financed by the Spanish MEC through project MAT-2003-01237 and the European Union Network of Excellence PHOREMOST (IST 511616). The authors gratefully acknowledge Dr. R. Serna for ellipsometric measurements on ZnO films.

 DOI: 10.1002/adma.200500569

ADVANCED MATERIALS

are the most appropriate approach for conformal infiltration, which allows a perfect replication of the template.

Here, we report a controlled process to fabricate large-area high quality ZnO–polystyrene (PS) composites and ZnO inverse opals with fine control over filling volume (nanometric in thickness) by a modified metal–organic chemical vapor deposition (MOCVD) method. Furthermore, once the ZnO structures are obtained, a sulfidation process is shown to be capable of producing ZnS inverse opals while maintaining the crystal quality of the original opal structures.

ZnO has been grown in thin PS opal[18] films on silicon substrates (500 nm sphere diameter and total thickness from 10 to 40 monolayers, 5–20 μm) by using a diluted solution of DMZn in hexane as zinc precursor. Double-distilled water (DDW) was used as oxygen precursor. The diluted metal–organic compound is easier to handle than the pure, highly reactive one. It also provides the key to fine control of the ZnO growth inside the opal. The two sources were kept separate in glass bubblers at room temperature. The precursors were alternately fed into the reactor using nitrogen as carrier gas at a fixed flow rate. Similar setups were used to grow SiO_2 in opals at room temperature.[19] In our case, the reactor was kept around 90 °C, which is a compromise temperature in order to obtain smooth deposits with fine grains while avoiding the softening of PS. Room temperature conditions yield rough and inhomogeneous deposits. The ZnO film thickness deposited by alternating exposure to the two sources in succession (a cycle) depends on the carrier gas flow rate, temperature, and exposure time of each source. Thus, a bare opal can be filled in a single cycle or in several cycles. This fact is of paramount importance in order to tune the photonic properties to the desired specifications for optimal performance. Most of the time, theory predicts particular or functional behavior for a given filling fraction. It is worth mentioning that due to the conformal growth and geometrical constrains the maximum value achievable for the filling fraction is close to 86 %. In addition, conformal growth permits the fabrication of inverse structures even for extremely low ZnO filling fractions.

Inverse opals were obtained upon calcination of PS-ZnO composites at 450 °C for 3 h in air. This process completely removes the PS matrix but also recrystallizes the ZnO, as will be discussed later. Scanning electron microscopy (SEM) inspections and optical spectroscopy have been performed in order to monitor the infiltration process and X-ray diffraction to confirm the crystal quality and composition of the deposits.

Figure 1 shows SEM images of ZnO-based opals grown on silicon substrates. Figure 1a shows the appearance of a cleaved edge of a ZnO–PS composite with an infiltration degree of 60 % of the pore volume. In this image, and due to the high contrast between conductive ZnO and the insulating PS spheres, the PS spheres are hardly visible, appearing as an inverse-like structure where the contact points between spheres can be observed as dark spots. Figures 1b,c show actual inverse ZnO opals from cleaved edges at different magnifications. The high quality of the smooth and homogeneous coating can be observed. Surface inspections reveal homogeneous

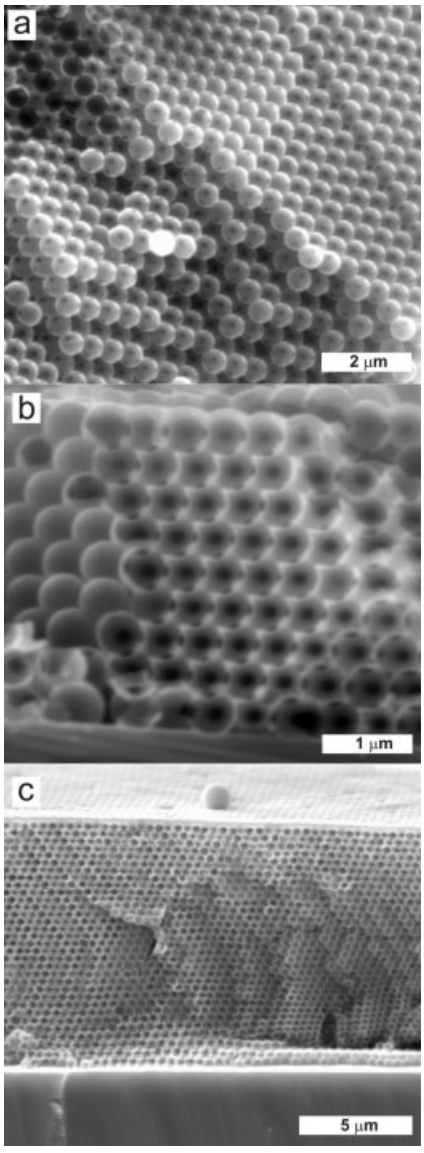

Figure 1. Images (SEM) of cleaved edges in ZnO infiltrated (a) and inverse (b,c) opal structures from 500 nm polystyrene spheres. The images allow the smoothness and quality of the conformal growth of ZnO shells, which extends for areas of hundreds of square micrometers, to be inferred.

growth over square-millimeter areas. The inverse replica order is disturbed only by the usual cracks (hundreds of micrometers apart) present in structures of this type, not by the ZnO growth. The empty interiors of the shells in the inverse replicas are observed only in cracks and the cleaved edges. From these we can give a rough estimate of the ZnO shell thickness of about 20–30 nm, in good agreement with the expected value. The elemental composition of the ZnO inverse structures was studied by energy dispersive X-ray analysis (EDX) (not shown). The absence of a carbon peak reveals the quantitative removal of PS.

By a sequence of several cycles it is possible to infill the opal with fine control of the filling fraction. The optical re-

sponses of ZnO–PS composites and ZnO inverse opals were compared with photonic band calculations.[20] The refractive index of opal-free ZnO films (0.4–1.6 μm) was measured by ellipsometric techniques to range from 2.2 to 1.9, in good agreement with data previously reported by Yoshikawa and Adachi.[21]

The infilling process has been monitored by the optical reflectance at near normal incidence with respect to the (111) face-centered cubic (fcc) planes taken with the help of an optical microscope from a circular area of about 375 μm diameter. The red-shift in the first-order Bragg peak as the infiltration proceeds accounts for the increase of the average refractive index of the structure due to ZnO infilling. Figure 2 shows the reflectance spectra for five CVD cycles. The bare PS opal spectrum (top) shows a peak with 55 % reflectivity at

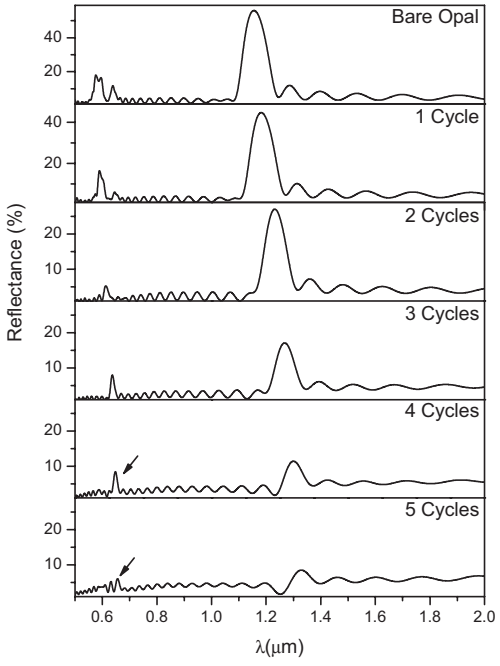

Figure 2. From top to bottom: Specular reflectance spectra for bare PS opal and five CVD cycles for ZnO infiltration. The Bragg peak shifts to higher wavelengths as the ZnO content increases. Notice Fabry–Perot ripples due to the opal thin film thickness (in this case around 5 μm). For high ZnO contents (cycles 4, 5) the reflectivity drops to values near 10 % due to the index-matching condition.

1160 nm, corresponding to the photonic pseudogap at the L point due to (111) planes. As the number of cycles increases, this peak moves to longer wavelengths (lower energies) up to a value of around 1330 nm. This latter value is hard to ascertain with precision because at values near 80 % of pore volume infiltration the average refractive index of the pore (ZnO/air) reaches that of the polystyrene (n = 1.57), producing an index-matching effect that hides the Bragg peak. However, high-energy features (around 0.6 μm) survive even at near index matching conditions (small arrows in Fig. 2), indicating the persistence of the photonic effects and the high quality of the structures.

By comparing these spectra with photonic band calculations we can estimate the ZnO grown in each CVD cycle. Figure 3 shows the filling volume and the associated layer thickness as a function of the number of cycles. As can be observed, ZnO

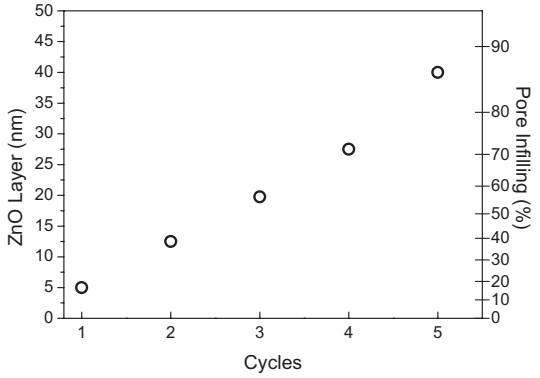

Figure 3. Evolution of the ZnO shell thickness around the PS spheres (left) and pore infilling (right, in percentage of the available volume) as a function of the number of cycles.

layer thickness increases with the number of cycles, from 5 nm in the first cycle (18 % of the pore volume) to about 40 nm for the last one (around 85 % of the pore volume). A linear fit of the experimental points indicates a growth rate of 8 nm per cycle, in good agreement with ellipsometric measurements for plain thin ZnO films. These figures give an idea of how fine this growth process is in terms of ZnO shell thickness control.

Optical properties of ZnO inverse structures have also been measured. Figure 4 shows the reflectance spectra of bare PS opal (b), ZnO–PS composite with 80 % pore volume infilling (c), and the same structure after PS calcination (d), together

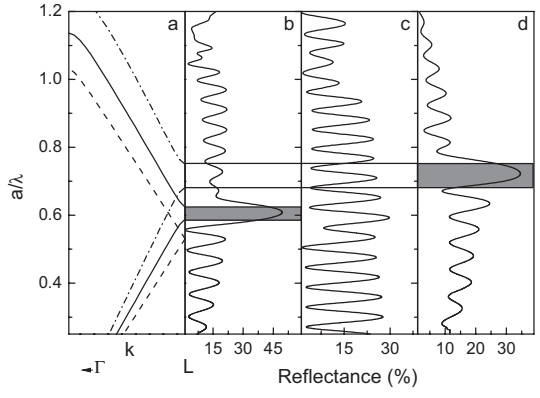

Figure 4. Specular reflectance spectra of a PS bare opal (b), 80 % ZnO–PS opal composite (c), and ZnO/air inverse structure (d), together with the corresponding photonic band calculations (a) for bare (solid), composite (dashed), and inverse (dashed-dotted) structures. Gray boxes indicate the corresponding photonic pseudogaps and are a guide for the eye.

ADVANCED MATERIALS

with photonic band calculations (a). The parameters used for the calculations were the following: for the bare opal PS spheres with a refractive index of n_{PS} = 1.59 were used arranged in a fcc lattice (solid line in Fig. 4a); for the ZnO infiltrated structure (dashed line in Fig. 4a) a layer of 30 nm around the PS spheres with a refractive index of n_{ZnO} = 1.93 (taken from ellipsometric data) was added; finally, for the inverse ZnO replica (dash-dotted line in Fig. 4a) the spheres' refractive index was replaced by 1 (air). As can be clearly seen from the spectra, in Figure 4c the Bragg peak disappears due to index matching (notice the disappearance of the pseudogap in the dashed line of (a)) and our system behaves as a homogeneous medium with a refractive index of around n_{av} = 1.65 and 5 μm thickness. After removal of PS by calcination the Bragg peak shifts to higher energies (blue-shifted), due to the lowering of the average refractive index (from n_{av} = 1.65 to n_{av} = 1.2), and becomes broader (almost double) because of the increase of the refractive index contrast (n_{ZnO}/n_{air} = 1.9).

In addition to this procedure to fabricate ZnO inverse opal structures, it is possible to go a step further. Sulfidation of ZnO is a method[22] that has been used to fabricate ZnS nanotubes recently.[23] Here, ZnO inverse opals can be sulfidated to produce ZnS inverse replicas.

X-ray diffraction was performed on ZnO–PS composites, ZnO inverse replicas, and ZnS after sulfidation, as can be seen in Figure 5. Figure 5a corresponds to an as-grown ZnO–PS composite, Figure 5b shows the X-ray diffractogram from the inverse ZnO opal after calcination, and Figure 5c corresponds

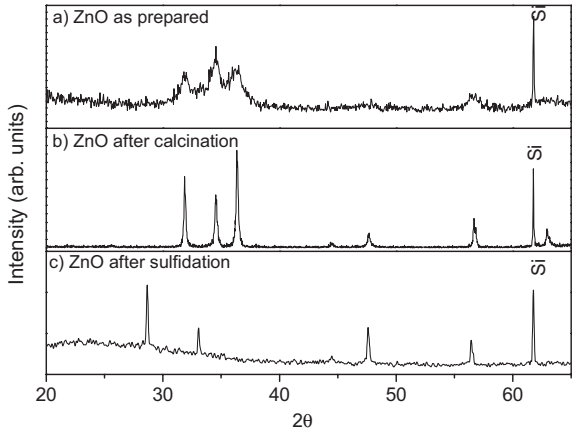

Figure 5. X-ray diffractograms from the ZnO–PS composite (a), ZnO inverse replica after calcination at 450 °C for 3 h (b), and ZnS inverse opal after sulfidation (c). The silicon reflection arises from the substrate.

to ZnS after sulfidation of the calcined ZnO opal. As can be observed, upon crystallization sharp peaks are obtained, in agreement with an increase in the grain size. All samples present a polycrystalline nature, the grain size[24] increasing from 4 to 40 nm upon calcination due to crystallization and to 53 nm after sulfidation due to 30 % difference in ZnS density, which provokes an increase of the semiconductor volume compared to that of ZnO.

This process can again be monitored by optical spectroscopy. In Figure 6 four specular reflectance spectra are shown, which correspond to bare PS opal (Fig. 6a); composite ZnO–PS opal with 60 % of the pore volume infiltrated (Fig. 6b); ZnO inverse opal after calcination (Fig. 6c); and ZnS inverse

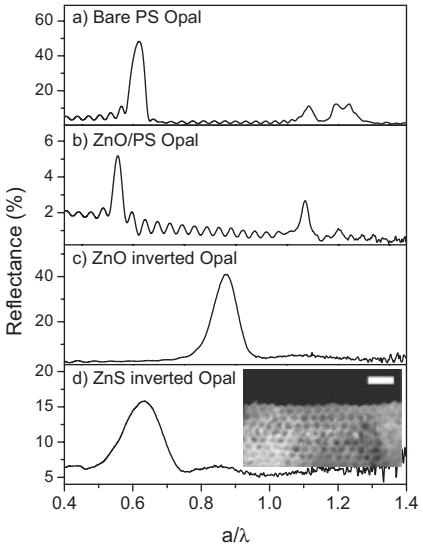

Figure 6. Specular reflectance for the bare opal (a), ZnO–PS composite (b), ZnO inverse opal (c), and ZnS after sulfidation (d). The inset in (d) shows a SEM image of a ZnS inverse opal (scale bar represents 1 μm).

structure after sulfidation of the previous (Fig. 6d). As expected, the Bragg peak centered at ca. 0.6 (in reduced units a/λ, where a is the lattice constant) for the bare PS opal, shifts to lower energy and narrows after ZnO infiltration. After calcination, this peak moves to higher energies due to lower average refractive index. After sulfidation, the peak moves again to lower energies for two reasons. Firstly, due to a 30 % specific volume increase from ZnO to ZnS, the lattice parameter grows by 10 %, which contributes to this red-shift. Secondly, the ZnS refractive index, n_{ZnS} = 2.3, is higher than that of ZnO. This latter fact also contributes to broadening of the peak due to a higher dielectric contrast. After the sulfidation process, and mainly due to this volume modification, the opal structure is slightly altered, as can be seen in the inset of Figure 6d. This may also be one of the reasons for this broadening and decrease in the reflectivity peak. This demonstrates not only that complete control over the photonic bandgap properties is provided by the infiltration procedure but also that the structures, even when shells as thin as 30 nm are synthesized, are robust enough to withstand inversion. This robustness makes them amenable to further chemical processing for regrowth or sulfidation as shown.

In summary, here we report the use of CVD to grow ZnO in synthetic opals. This method yields large-area, high-quality ZnO–PS and ZnO inverse opals with very precise control of degree of infiltration, which, in terms of thickness, means nanometer-thick layers. For the quality of the deposits and the

ease of use, as well as for its inexpensiveness, this may well turn out to be the ultimate method of synthesis for a material that has gained a place on the rostrum of materials for photonics. It is also shown that further chemical processing can be performed to obtain ZnS inverse opals of the same quality that enrich the properties of the system and add to the potential of the method.

Experimental

ZnO infiltration was performed following a CVD method based on a similar procedure described in the literature [19]. The two reactants were alternately transported by a N_2 flow from two separate bubblers. The flow carried the vapor phases to the reactor containing the sample. The reactor was kept at 90 °C approximately.

In a typical run double-distilled water was bubbled by a N_2 carrier gas at a rate of 200 mL/min in a pre-treatment step in order to moisten the reactor for 3–5 min. After that, the sample was placed in the reactor and water was again bubbled for periods ranging from 30 to 120 s (200 mL/min N_2 flow). Next, the container with the metal–organic compound was bubbled (150 mL/min N_2 flow) for periods ranging from 15 to 30 s. After the sample had been removed, a N_2 purge (200 mL/min) was used to rid the setup of possible residues as a preparatory step to a new cycle. Dimethyl zinc 95 % minimum (10 wt.-% in hexane) was purchased from ABCR GmbH & Co. KG.

For the sulfidation processing both the ZnO inverse opals and sulfur powder (0.025 g) were placed inside a glass ampoule sealed in vacuum. The ampoule was then ramped at 1 °C/min up to 450 °C and kept at that temperature for 10 h, which provided a sulfur atmosphere of 500 torr (~67 kPa).

The X-ray powder diffraction study was carried out in a Bruker D8 advance from Bruker-axs GmbH using Cu Kα radiation.

The SEM inspection was performed without further metallic films covering the samples.

Optical characterization was performed in a Fourier transform infrared spectrometer, IFF 66S from Bruker, with an IR Scope II microscope attached. All reflectance spectra were recorded at near-normal incidence to the (111) family of planes. All compared spectra were taken at the same sample spot.

Received: March 17, 2005
Final version: June 7, 2005
Published online: September 29, 2005

Note added in proof: M. Scharrer et al. have independently obtained ZnO inverted opals by atomic layer deposition.[25]

[1] D. C. Look, *Mater. Sci. Eng. B* **2001**, *80*, 383.
[2] Z. K. Tang, G. K. L. Wong, P. Yu, M. Kawasaki, A. Ohtomo, H. Koinuma, Y. Segawa, *Appl. Phys. Lett.* **1998**, *72*, 3270.
[3] a) Y. Li, G. W. Meng, L. D. Zhang, F. Phillipp, *Appl. Phys. Lett.* **2000**, *76*, 2011. b) M. H. Huang, S. Mao, H. Feick, H. Q. Yan, Y. Y. Wu, H. Kind, E. Weber, R. Russo, P. D. Yang, *Science* **2001**, *292*, 1897.
[4] Z. W. Pan, Z. R. Dai, Z. L. Wang, *Science* **2001**, *291*, 1947.
[5] a) B. D. Yao, Y. F. Chan, N. Wang, *Appl. Phys. Lett.* **2002**, *81*, 757. b) P. X. Gao, Z. L. Wang, *J. Phys. Chem. B* **2002**, *106*, 12 653.
[6] C. López, *Adv. Mater.* **2003**, *15*, 1679.
[7] M. C. Larciprete, C. Sibilia, S. Paoloni, M. Bertolotti, F. Sarto, M. Scalora, *J. Appl. Phys.* **2003**, *93*, 5013.
[8] X. Wu, A. Yamilov, X. Liu, S. Li, V. P. Dravid, R. P. H. Chang, H. Cao, *Appl. Phys. Lett.* **2004**, *85*, 3657.
[9] E. W. Seelig, B. Tang, A. Yamilov, H. Cao, R. P. H. Chang, *Mater. Chem. Phys.* **2003**, *80*, 257.
[10] S. M. Abrarov, Sh. U. Yuldashev, S. B. Lee, T. W. Kang, *J. Lumin.* **2004**, *109*, 25.
[11] V. V. Ursaki, I. M. Tiginyanu, V. V. Zalamai, V. M. Masalov, E. N. Samarov, G. A. Emelchenko, F. Briones, *J. Appl. Phys.* **2004**, *96*, 1001.
[12] H. Yan, C. F. Blanford, J. C. Lytle, C. B. Carter, W. H. Smyrl, A. Stein, *Chem. Mater.* **2000**, *12*, 1134.
[13] T. Sumida, Y. Wada, T. Kitamura, S. Yanagida, *Chem. Lett.* **2001**, *1*, 38.
[14] a) T. Suntola, J. Hyvarinen, *Annu. Rev. Mater. Sci.* **1985**, *15*, 177. b) S. M. George, A. W. Ott, J. W. Klaus, *J. Phys. Chem.* **1996**, *100*, 13 121.
[15] M. Ritala, M. Leskela, J. Dekker, C. Mutsaers, P. J. Soininen, J. Skarp, *Chem. Vap. Deposition* **1999**, *5*, 7.
[16] J. W. Elam, Z. A. Sechrist, S. M. George, *Thin Solid Films* **2002**, *414*, 43.
[17] B. Sang, M. Konagai, *Jpn. J. Appl. Phys., Part 2* **1996**, *35*, L602.
[18] P. Jiang, J. F. Bertone, K. S. Hwang, V. L. Colvin, *Chem. Mater.* **1999**, *11*, 2132.
[19] H. Míguez, N. Tétreault, B. Hatton, S. M. Yang, D. Perovic, G. A. Ozin, *Chem. Commun.* **2002**, 2736.
[20] S. G. Johnson, J. D. Joannopoulos, *Opt. Express* **2001**, *8*, 173.
[21] H. Yoshikawa, S. Adachi, *Jpn. J. Appl. Phys., Part 1* **1997**, *36*, 6237.
[22] S. Lew, A. F. Sarofim, M. Flytzanistephanopoulos, *Ind. Eng. Chem. Res.* **1992**, *31*, 1890.
[23] L. Dloczik, R. Engelhardt, K. Ernst, S. Fiechter, I. Sieber, R. Konenkamp, *Appl. Phys. Lett.* **2001**, *78*, 3687.
[24] Data are an estimate obtained by applying the Scherrer formula.
[25] M. Scharrer, X. Wu, A. Yamilov, H. Yamilov, H. Cao, R. P. H. Chang, *Appl. Phys. Lett.* **2005**, *86*, 151 113.

The Dynamics of Nanowire Self-Assembly**

By *Min Chen* and *Peter C. Searson**

The bottom–up approach to device fabrication involves the synthesis and assembly of nanoscale building blocks. Assembly is usually achieved through electrostatic or chemical interactions between the individual building blocks or through interaction with an external electric or magnetic field. In more sophisticated approaches, the building blocks can be functionalized with molecules whose end groups will only bind specifically to other particles functionalized with a complementary group. Such receptor-mediated interactions have been exploited for the self-assembly of spherical nanoparticles.[1,2] The assembly of more complex structures requires the ability to control the shape, composition, and surface chemistry of

[*] Prof. P. C. Searson, M. Chen
Department of Materials Science and Engineering
Johns Hopkins University
Baltimore, MD 21218 (USA)
E-mail: searson@jhu.edu

[**] This work was supported by the David and Lucile Packard Foundation (grant number 2001-17715) and the DARPA Biomagnetics Program (DARPA/AFOSR grant number F49620-02-1-0307).

 DOI: 10.1002/adma.200501292